Path instability of a no-slip spheroidal bubble in isotropic turbulence

Gihun Shim ⊙[*] and Jongsu Kim ⊙

School of Mathematics and Computing, Yonsei University, Seoul, 03722, Korea

Changhoon Lee[†]

School of Mathematics and Computing, Yonsei University, Seoul, 03722, Korea
and Department of Mechanical Engineering, Yonsei University, Seoul, 03722, Korea

Path instability of a millimetric spheroidal bubble in quiescent fluid and in isotropic turbulence is investigated by direct numerical simulation. An immersed boundary method along with a new formulation of the equation of bubble motion is utilized to impose the no-slip condition on the surface of an air bubble in fixed shape with the equivalent diameter of $1.0 \sim 4.0$ mm in contaminated water. The range of Galilei number defined as the ratio of the gravitational force to the kinematic viscosity considered in this study is $100 \sim 800$. In still fluid, as the bubble size grows, the frequency of the zigzagging motion of the bubble increases while the range in the orientation angle variation of the bubble is hardly affected. The effect of background turbulence on path instability of a rising bubble, which typically shows zigzag pattern in still fluid, is investigated at three different Reynolds numbers, Re_λ, of 26, 45, and 73, or equivalently, for the ratio of fluid root-mean-square velocity to the bubble rise velocity u'/V_T ranging $0.030 \sim 0.671$. When a bubble rises in isotropic turbulence, the terminal rise velocity of the bubble does not show a noticeable difference. However, the pathways are significantly distorted by turbulence. Furthermore, the magnitude of zigzagging frequency and the degree of obliquity of the bubble become enhanced with Re_λ. We also observed wakes behind the bubble to find that the rear tails become weaker and tangled due to turbulence.

I. INTRODUCTION

Bubble dynamics has been widely studied for many industrial applications ranging from water purification process, fluidized bed reactors for promoting catalysts to be dissolved, prevention from cavitational woes, reduction of bubbles attached to cladding conduits in atomic piles to name a few. For successful applications of bubbles, the behavior of bubbles in various environments needs to be properly understood. Especially, one of the representative features of a millimetric bubble is path instability exhibiting distorted pathways such as zigzagging or helical motion as it rises in fluid. The path instability mainly arises from asymmetric wake formation behind the bubble, shape oscillation, and surfactant concentration on surface Magnaudet and Eames [1]. In fact, a variety of studies have been carried out to investigate the path instability of a bubble using numerical simulations or experiments. For example, Wu and Gharib [2] tracked a millimetric bubble in clean stagnant water. They suggested the critical Reynolds number and the corresponding aspect ratio for a transition to zigzagging and helical motions. Riboux *et al.* [3] also showed helical vestiges of a bubble with its

---

[*]lingenious2@gmail.com

[†]clee@yonsei.ac.kr

rise velocity and provided a specific Reynolds number at which those helical motions started. Shew *et al.* [4] identified the path transition from rectilinear through zigzagging, and up to helical motions from bubble rise velocities, concluding that the rise velocity oscillates in the zigzagging regions and becomes almost constant in the helical regions. A contribution to path instability by shape oscillation was also addressed by Lunde and Perkins [5], who reported that the form of a bubble was changed to a wobbly shape either elongated or contracted axially when the shape oscillation occurred due to fluidic pressure surrounding the bubble.

Veldhuis *et al.* [6] carried out further investigation about how a bubble path was changed under the shape variation, reporting that the bubble showed a smaller path oscillation frequency as it grew. They also proposed an inversely proportional correlation between the bubble size and the wake frequency of fluid proximate to the bubble. Surfactant concentration affects the surface tension of a bubble, and thus its aspect ratio and rise velocity are distinct from those of a surfactant-free bubble. Clift *et al.* [7] depicted an overall picture between the terminal velocity of a bubble and its size for both clean and contaminated water. Tagawa *et al.* [8] conducted experiments to observe how the path of a bubble was changed according to the surfactant concentration. They reported that a helical path was transformed into a zigzagging path as the concentration was increased. Tagawa *et al.* [9] also addressed that the drag coefficient was in decline during an increase in the surfactant concentration, and they classified types of the bubble path according to the drag coefficient.

Numerical simulations have also been carried out to describe the dynamics of a bubble. Tripathi *et al.* [10] classified bubble paths and shapes through Eötvös and Galilei numbers from which this taxonomy was significant for better understandings of the physical traits. Mougin and Magnaudet [11], Shew and Pinton [12] displayed a path transition of a clean bubble from zigzagging motions to helical ones by solving generalized Kirchhoff equations Mougin and Magnaudet [13]. Cano-Lozano *et al.* [14] described a series of changes of wake instability behind the realistic bubble by applying the no-slip boundary condition on the surface. They observed that zigzagging paths occur after distortion of wake symmetry appeared. Recently, Cano-Lozano *et al.* [15] investigated more details of paths and wakes for various types of deformable bubbles in stagnant fluid. They sorted path regimes of the bubble through utilizing the Eötvös and Galilei numbers similarly to Tripathi *et al.* [10], which was also useful for understanding an overall view of the path characteristics.

As discussed, the path instability has been investigated in many ways. Most researches, however, are confined to bubbles in still fluid although in many real applications the background flow is often turbulent. Recently, Mathai *et al.* [16] experimentally investigated dispersion of millimetric air bubbles in homogeneous isotropic turbulence and attributed the early transition to diffusive dispersion of bubbles to path instability. Kim *et al.* [17] measured pair dispersion of millimetric air bubbles in Rayleigh–Benard convection in a cubic box and observed that the horizontal pair dispersion is enhanced for large initial separations although convection tends to suppress path instability. Several numerical simulations were performed considering dynamics of bubbles and light particles in turbulence [18–23]. Still, how the background turbulence affects path instability of a millimetric bubble is not fully understood. Therefore, we in this paper investigate how the behavior of a bubble is modified by turbulence. For this purpose, we studied the behavior of a single bubble of the millimetric size in isotropic turbulence using direct numerical simulation. To reflect more realistic circumstances of the bubble, we considered an oblate spheroidal air bubble with size ranging $1.0 \sim 4.0$ mm. It is assumed that the bubble has a fixed shape and is put in fully contaminated water. Due to the high concentration of surfactants, the no-slip boundary condition is satisfied on its surface [7,9,24].

The organization in our paper follows. In Sec. II, numerical procedures are introduced to solve the equations of motion of a single bubble by adopting an immersed boundary method. In Sec. III, we analyze bubble paths and statistics related to zigzag patterns in still fluid. In Sec. IV, we discuss the similar statistics of the bubble in three kinds of isotropic turbulence at $\mathrm{Re}_\lambda = 26$, 45, and 73. Finally, in Sec. V, an overall summary of the current study is provided.

II. METHODOLOGY TO DESCRIBE THE MOTION OF A SPHEROIDAL BUBBLE

To describe dynamics of a spheroidal bubble in fluid through direct numerical simulation, we utilize an immersed boundary method (IBM) to efficiently handle the interaction between a bubble and the background flows. In this section, we introduce a numerical methodology to implement IBM based on a direct forcing scheme. A new form of the equations of motion of a bubble was derived using an explicit formula for the moment of inertia matrix for a spheroidal bubble and was solved through the application of a virtual mass term added on both sides of the governing equation, which is used for obviating singularity caused by extremely low mass of a bubble. Details are provided in the following subsections.

A. Governing equations for a single bubble in fluid

For the simulation of background turbulent flow, we solve three-dimensional Navier–Stokes equations and continuity equation:

$$\frac{\partial \boldsymbol{u}}{\partial t} + (\boldsymbol{u} \cdot \boldsymbol{\nabla})\boldsymbol{u} = -\frac{1}{\rho_f}\boldsymbol{\nabla}P + \nu\nabla^2\boldsymbol{u} + \boldsymbol{f}_b + \boldsymbol{f}_L, \tag{1}$$

$$\boldsymbol{\nabla} \cdot \boldsymbol{u} = 0, \tag{2}$$

where $\boldsymbol{u}$, ρ_f, P, ν, $\boldsymbol{f}_b$, $\boldsymbol{f}_L$ denote the fluid velocity, density of fluid, modified pressure, kinematic viscosity, back reaction force of a bubble onto fluid, and large-scale forcing maintaining turbulence, respectively. Equations (1) and (2) were solved using a pseudo-spectral method in a rectangular parallelepiped domain of size $L_h \times L_h \times L_v$ where L_h and L_v denote the horizontal and vertical extents of the domain, respectively. Periodicity was assumed in all three directions and L_v/L_h was chosen to be 16 to accommodate a rising single bubble, minimizing the effect of periodicity assumption. $\boldsymbol{f}_L$ can be obtained from the stochastic differential equation (SDE) which satisfies the Langevin equation with a time scale T and standard deviation σ [25]:

$$dU(t) = -\frac{U(t)}{T}\,dt + \left(\frac{2\sigma^2}{T}\right)^{1/2}dW, \tag{3}$$

where U and W denote the Uhlenbeck-Ornstein stochastic process, and the Wiener process, respectively. dW is chosen from Gaussian distribution with zero mean and variance dt. Then, a three-dimensional complex vector in Fourier space $\hat{\boldsymbol{b}}(\boldsymbol{k})$ can be constructed using six independent Uhlenbeck-Ornstein processes:

$$\hat{\boldsymbol{b}} = \begin{pmatrix} U_1 \\ U_2 \\ U_3 \end{pmatrix} + i\begin{pmatrix} U_4 \\ U_5 \\ U_6 \end{pmatrix}. \tag{4}$$

Note that $\hat{\boldsymbol{b}}$ is nonzero in the range $0 < |\boldsymbol{k}| \leqslant k_f$ where $\boldsymbol{k}$ and k_f denote the wavenumber vector and maximum forcing wavenumber, respectively. Finally, we can derive $\hat{\boldsymbol{f}}_L$ in Fourier space, which ensures the divergence-free condition,

$$\hat{\boldsymbol{f}}_L = \hat{\boldsymbol{b}} - \boldsymbol{k}(\boldsymbol{k} \cdot \hat{\boldsymbol{b}})/(\boldsymbol{k} \cdot \boldsymbol{k}). \tag{5}$$

Detailed algorithm including the forcing scheme for $\boldsymbol{f}_L$ is provided in Jung *et al.* [26] and the same code has been used for various studies of particle-laden turbulence [27–32].

In our study, we did not consider the dynamic effect of surface tension on the surface of the bubble. Instead, the effect of surface tension is implemented into the fixed spheroidal shape of the bubble. The motion of a bubble without shape variation can be solved through equations of linear and angular motions [33,34]. Especially, we adopt the no-slip boundary condition on the bubble surface due to the assumption of the fully contaminated bubble, which is illustrated in more detail

in the next subsection. The equations for the translational and angular motions of a bubble with bubble domain Ω follow

$$\rho_b V_b \frac{d\boldsymbol{v}_c}{dt} = -\rho_f \int_\Omega \boldsymbol{F} dV + \rho_f \frac{d}{dt} \int_\Omega \boldsymbol{u} dV + (\rho_b - \rho_f)V_b \boldsymbol{g}, \tag{6}$$

$$\frac{d(I_b \boldsymbol{\omega}_c)}{dt} = -\rho_f \int_\Omega (\boldsymbol{X}_l - \boldsymbol{x}_c) \times \boldsymbol{F}(\boldsymbol{X}_l) dV + \rho_f \frac{d}{dt}\left[\int_\Omega (\boldsymbol{x} - \boldsymbol{x}_c) \times \boldsymbol{u}(\boldsymbol{x}) dV\right], \tag{7}$$

where ρ_b, V_b, $\boldsymbol{v}_c$, $\boldsymbol{F}$, $\boldsymbol{g}$ in Eq. (6) represent the density of the bubble, the bubble volume, velocity vector of the bubble at its center, IBM force exerted onto the bubble surface by fluid, and gravitational acceleration vector, respectively. I_b, $\boldsymbol{\omega}_c$, X_l, $\boldsymbol{x}_c$, $\boldsymbol{x}$ in Eq. (7) are the moment of inertia matrix of a spheroidal bubble, angular velocity of the bubble at its center, the position of the Lagrangian points on the bubble surface for IBM implementation, displacement vector of the bubble center, and Eulerian points in the bubble domain, respectively. However, since the density ratio $\pi_b (= \rho_b/\rho_f)$ is much smaller than 1, a direct numerical implementation of Eqs. (6) and (7) causes a singular problem. To resolve this, we employed a virtual mass force to both equations [35],

$$\left(1 + \frac{C_v}{\pi_b}\right)\rho_b V_b \frac{d\boldsymbol{v}_c}{dt} = -\rho_f \int_\Omega \boldsymbol{F} dV + \rho_f \frac{d}{dt} \int_\Omega \boldsymbol{u} dV + (\rho_b - \rho_f)V_b \boldsymbol{g} + C_v \rho_f V_b \frac{d\boldsymbol{v}_c}{dt}, \tag{8}$$

$$\left(1 + \frac{C_v}{\pi_b}\right)\frac{d(I_b \boldsymbol{\omega}_c)}{dt} = -\rho_f \int_\Omega (\boldsymbol{X}_l - \boldsymbol{x}_c) \times \boldsymbol{F}(\boldsymbol{X}_l) dV + \rho_f \frac{d}{dt}\left[\int_\Omega (\boldsymbol{x} - \boldsymbol{x}_c) \times \boldsymbol{u}(\boldsymbol{x}) dV\right] + \frac{C_v}{\pi_b}\frac{d(I_b \boldsymbol{\omega}_c)}{dt}, \tag{9}$$

where C_v is an arbitrary coefficient which is chosen to be 0.5 in the present study.

It is noted that $I_b(t)$ for a spheroid as given below evolves with the bubble's orientation unit vector $\boldsymbol{p}(t)$, which is defined in the direction along the symmetry axis of a spheroid,

$$I_b = \frac{2\rho_b V_b r_b^2 \boldsymbol{pp}}{5} + \frac{\rho_b V_b (r_a^2 + r_b^2)(I - \boldsymbol{pp})}{5}, \tag{10}$$

where r_a is the radius of a spheroid along the symmetry axis, r_b is the radius in the direction normal to the symmetry axis, with $r_a < r_b$ indicating an oblate spheroid used in this study. I is the identity matrix. The orientation vector $\boldsymbol{p}(t)$ of the bubble evolves in time by

$$\frac{d\boldsymbol{p}}{dt} = \boldsymbol{\omega}_c \times \boldsymbol{p}, \tag{11}$$

indicating that $|\boldsymbol{p}(t)| = 1$ is always maintained. Ardekani *et al.* [36] introduced an iterative algorithm to solve Eq. (7) to handle time-varying $I_b(t)$. However, by noticing that the inverse of I_b can be explicitly obtained [37,38],

$$I_b^{-1} = \frac{5\boldsymbol{pp}}{2\rho_b V_b r_b^2} + \frac{5(I - \boldsymbol{pp})}{\rho_b V_b (r_a^2 + r_b^2)}, \tag{12}$$

we reformulated Eq. (9),

$$\left(1 + \frac{C_v}{\pi_b}\right)\frac{d(I_b \boldsymbol{\omega}_c)}{dt} = \left(1 + \frac{C_v}{\pi_b}\right)\left(I_b \frac{d\boldsymbol{\omega}_c}{dt} + \frac{dI_b}{dt}\boldsymbol{\omega}_c\right) = \boldsymbol{T}, \tag{13}$$

where $\boldsymbol{T}$ is the right-hand side of Eq. (9), from which

$$\frac{d\boldsymbol{\omega}_c}{dt} = -I_b^{-1}\frac{dI_b}{dt}\boldsymbol{\omega}_c + \frac{1}{1 + C_v/\pi_b}I_b^{-1}\boldsymbol{T}. \tag{14}$$

Using Eqs. (10), (11), and (12), we finally derived

$$\frac{d\boldsymbol{\omega_c}}{dt} = -\frac{r_b^2 - r_a^2}{r_b^2 + r_a^2}(\boldsymbol{\omega_c} \cdot \boldsymbol{p})\boldsymbol{\omega_c} \times \boldsymbol{p} + \frac{1}{1 + C_v/\pi_b}I_b^{-1}$$
$$\times \left(-\rho_f \int_\Omega (\boldsymbol{X_l} - \boldsymbol{x_c}) \times \boldsymbol{F}(\boldsymbol{X_l})dV + \rho_f \frac{d}{dt}\left[\int_\Omega (\boldsymbol{x} - \boldsymbol{x_c}) \times \boldsymbol{u}(\boldsymbol{x})dV \right] + \frac{C_v}{\pi_b}\frac{d(I_b\boldsymbol{\omega_c})}{dt} \right).$$

$$(15)$$

For the IBM implementation, the surface coordinates of a spheroidal bubble were searched using the rotational matrix between the absolute frame and bubble fixed frame $\boldsymbol{x}'$,

$$\boldsymbol{x} - \boldsymbol{x_c} = R\boldsymbol{x}', \tag{16}$$

where on the surface of the bubble, $\boldsymbol{x}'$ satisfies

$$\frac{x'^2}{r_a^2} + \frac{y'^2 + z'^2}{r_b^2} = 1. \tag{17}$$

The rotational matrix R is constructed by

$$R = (\boldsymbol{i_1} : \boldsymbol{i_2} : \boldsymbol{i_3})(\boldsymbol{i_1'} : \boldsymbol{i_2'} : \boldsymbol{i_3'})^t, \tag{18}$$

where $\boldsymbol{i_1}, \boldsymbol{i_2}, \boldsymbol{i_3}$ are the unit directional vectors in the absolute frame, while $\boldsymbol{i_1'}, \boldsymbol{i_2'}, \boldsymbol{i_3'}$ are the unit directional vectors in the bubble fixed frame, which can be constructed from $\boldsymbol{p}(t)$ by TRIAD (Three-axis attitude determination) method [39],

$$\boldsymbol{i_1'} = \boldsymbol{p}, \boldsymbol{i_2'} = \frac{\boldsymbol{p} \times \boldsymbol{q}}{|\boldsymbol{p} \times \boldsymbol{q}|}, \boldsymbol{i_3'} = \boldsymbol{i_1'} \times \boldsymbol{i_2'}, \tag{19}$$

where $\boldsymbol{q}$ is an arbitrary vector.

B. Immersed boundary method

To impose the no-slip boundary condition on the surface of the bubble in contaminated water, we adopted an immersed boundary method which is an efficient method for the simulation of a moving object in fluid without an introduction of body-fitted coordinates. Uhlmann [40], Kempe and Fröhlich [41] introduced the IBM based on a direct forcing scheme, which can impose a desired velocity on the object surface and the back reaction force from its surface exerts explicitly to proximate Eulerian grids. Tschisgale *et al.* [42] proposed a semi-implicit scheme to release stability thresholds, producing good agreement for a heavy and light particle compared to previous IBM results. Tavanashad and Subramaniam [43] simulated the motion of a single spherical bubble in still fluid with the direct forcing and virtual mass forces, which showed well-fitted drag coefficients compared to other simulations and experiments.

On the other hand, many sorts of turbulence modification by finite-sized particles have been studied using various forms of IBM. Yeo *et al.* [44] investigated impact of particles on isotropic turbulence, reporting an enhancement of small scales of turbulence at high wavenumbers regardless of the density of particles. Tanaka and Teramoto [33] investigated modulation of shear turbulence by finite-sized heavy particles through IBM, proving that the presence of particle led to kinetic energy enhancement. Jang [38], Jang and Lee [45,46] developed an IBM which can be applied to nonuniform grids and observed impacts of an increase in the number of finite-sized particles on stratified turbulence, which enhanced internal gravity waves in channel center region and vortex structures became weaker in the near-wall regions. Derksen [47] confirmed using an IBM that the aggregation size of spherical particles was dependent on particle-particle interactions and intensity of turbulence. Fornari *et al.* [48] reported a significantly reduced settling velocity of slightly heavy spherical particles under isotropic turbulence when compared to that in still fluid. Tanaka [34,49]
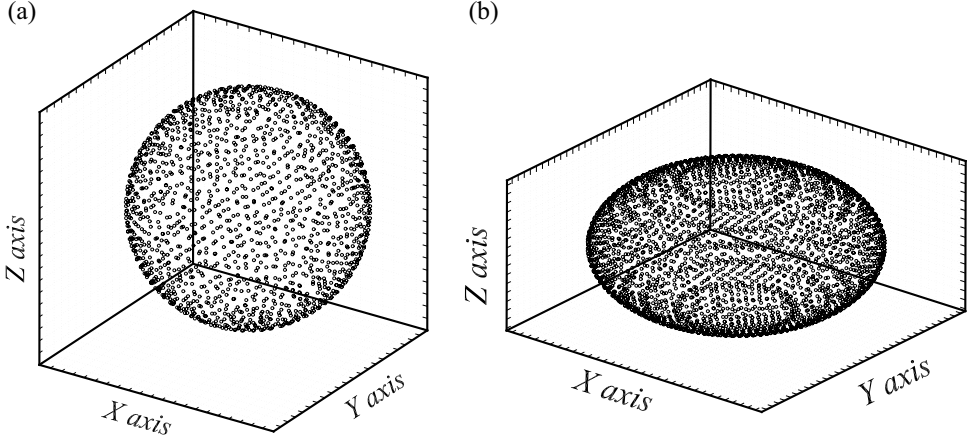
FIG. 1. Distribution of Lagrangian points for (a) a sphere ($\chi = 1$) with $N_l = 1588$, (b) an oblate spheroid ($\chi = 2$) with $N_l = 2976$. The points are allocated on each cell along the surface in horizotnal x, y axes and vertical z axis.

accounted for spherical sediments and bubbles in shear turbulence, and described how the turbulence was modified by particles and bubbles.

In our study, we adopted an IBM based on the direct forcing scheme. The sequence to apply the IBM is as follows. First, we place the Lagrangian points (X_l) on the surface of the bubble (see Fig. 1, for example) under the principle that one Lagrangian point is allocated to one Eulerian grid cell. Detailed algorithm for the distribution of the Lagrangian points can be found in Jang [38], Jang and Lee [45]. The velocity information at the Lagrangian point is extracted from the nearby Eulerian information as follows:

$$U_l(X_l) = \sum_{x \subset \Omega} u(x) w(X_l - x), \tag{20}$$

where $w(X_l - x)$ is the interpolation weight. Then, the immersed boundary force $F(X_l)$ at the Lagrangian point X_l is computed by

$$F(X_l) = \frac{U_d(X_l) - U_l(X_l)}{\Delta t}, \tag{21}$$

where $U_d(X_l)$ is the desired velocity at the Lagrangian point determined by the motion of the bubble, $U_d(X_l) = v_c + \omega_c \times (X_l - x_c)$. Finally, the forcing at the nearby Eulerian grid points f_b of Eq. (1) is obtained by

$$f_b(x) = \sum_{l=1}^{N_l} F(X_l) w'(X_l - x), \tag{22}$$

where $w'(X_l - x)$ is the distribution weights. The interpolation weights $w(X_l - x)$ and distribution weights $w'(X_l - x)$ are determined by the conservation of force and moment [50],

$$\sum_{x \subset \Omega} f_b(x) \Delta V_h = \sum_{l=1}^{N_l} F(X_l) \Delta V_l, \tag{23}$$

$$\sum_{x \subset \Omega} (x - x_c) \times f_b(x) \Delta V_h = \sum_{l=1}^{N_l} (X_l - x_c) \times F(X_l) \Delta V_l, \tag{24}$$

TABLE I. Cases for a single bubble rising in quiescent fluid conducted in our simulation. The range of the parameters correspond to a fully contaminated bubble considered in Ref. [7]. The range of Ga and χ are chosen for the real sizes of an air bubble ranging from $1.0 \sim 4.0$ mm. h is the numerical grid size. The zigzagging amplitude A from its dominant horizontal view, minimal and maximal inclination degrees, $\theta_{\min}$, $\theta_{\max}$ in the dominant horizontal axis are measured.

Case	d_e(mm)	Ga	χ	d_e/h	d_e/L_h	N_l	Re_b	C_d	St_r	A/d_e	$\theta_{\min}$	$\theta_{\max}$
$S-1.0$	1.0	99.0	1.03	18.7	0.097	1645 ± 5	107	1.14	0	0	$5°$	$5°$
$S-1.5$	1.5	182.0	1.06	19.1	0.099	1712 ± 6	218 ± 1	0.94	0.094	0.22	$1°$	$19°$
$S-2.0$	2.0	280.1	1.10	26.1	0.136	3205 ± 8	309 ± 13	1.08	0.114	0.84	$-19°$	$30°$
$S-2.5$	2.5	391.5	1.14	30.0	0.156	4250 ± 12	407 ± 29	1.19	0.130	0.88	$-24°$	$35°$
$S-3.0$	3.0	514.6	1.18	37.5	0.195	6665 ± 15	512 ± 44	1.34	0.143	0.87	$-30°$	$37°$
$S-3.5$	3.5	648.5	1.22	38.4	0.218	6985 ± 19	624 ± 57	1.47	0.153	0.83	$-30°$	$37°$
$S-4.0$	4.0	792.5	1.28	43.3	0.225	8880 ± 25	756 ± 66	1.59	0.168	0.78	$-30°$	$37°$

where ΔV_l and ΔV_h are volume allocated to each Lagrangian point and the Eulerian cell volume. From Eqs. (23) and (24), the following relation between the weight functions w and w' hold

$$w(\boldsymbol{X}_l - \boldsymbol{x})\Delta V_l = w'(\boldsymbol{X}_l - \boldsymbol{x})\Delta V_h. \tag{25}$$

For the choice of interpolation function, Roma *et al.* [51] implemented the dirac delta function and verified no difference in accuracy compared to other choices. In our study, the four-points Lagrange interpolation function was utilized.

III. ZIGZAGGING MOTIONS OF A SPHEROIDAL BUBBLE IN STILL FLUID

It is well known that the motions of a fully contaminated bubble show zigzagging patterns when it rises in still fluid [1,8]. Before an investigation on how the motion of a bubble is modified by turbulence, we study the motion of a bubble in still fluid with a focus on the behavior of a bubble of various sizes with a purpose of validation of our numerical method. The nondimensional parameters involved in the bubble motion are introduced as follows:

$$Ga = \frac{\left(|\pi_b - 1|gd_e^3\right)^{1/2}}{\nu}, \quad \chi = \frac{r_b}{r_a}, \tag{26}$$

where Ga, χ, and d_e denote Galilei number, bubble aspect ratio, equivalent diameter of a bubble defined by $d_e = 2(r_a r_b^2)^{1/3}$, respectively. In our simulations, we put $\pi_b = 10^{-3}$ to consider an infinitesimal mass of the bubble. To discuss dynamics of the bubble, we introduce

$$Re_b = \frac{V_T d_e}{\nu}, \quad St_r = \frac{f d_e}{V_T}, \tag{27}$$

where Re_b, St_r, V_T and f indicate bubble Reynolds number, Strouhal number, its averaged rise velocity, and path oscillation frequency, respectively. As many studies have shown, the averaged χ can be determined by Eötvös number $Eo = \rho_b g d_e^2 / \sigma$ where σ is surface tension coefficient of the bubble [7,52]. Aoyama *et al.* [54] also established χ by a combination of Eo and Re_b, which showed good agreement in their experiments. Therefore, in our study we adopted the values of χ for different sizes of the bubble. Table I lists seven simulation cases for the bubble diameters ranging from $1.0 \sim 4.0$ mm with an interval of 0.5 mm. The viscosity of the fluid is $\nu = 0.01$ cm^2/s, and $g = 981$ cm/s^2 in real units. To conduct efficient simulations of a single bubble rising, a periodic rectangular parallelepiped domain with $L_v/L_h = 16$ is utilized. The corresponding grid numbers are 128 and 2048 for the horizontal and vertical directions, respectively. Nineteen to 43 grids are allocated to an equivalent diameter of a bubble depending of the size as shown in Table I, which seems to be sufficient for resolving the bubble shape. The horizontal extent of the simulation domain
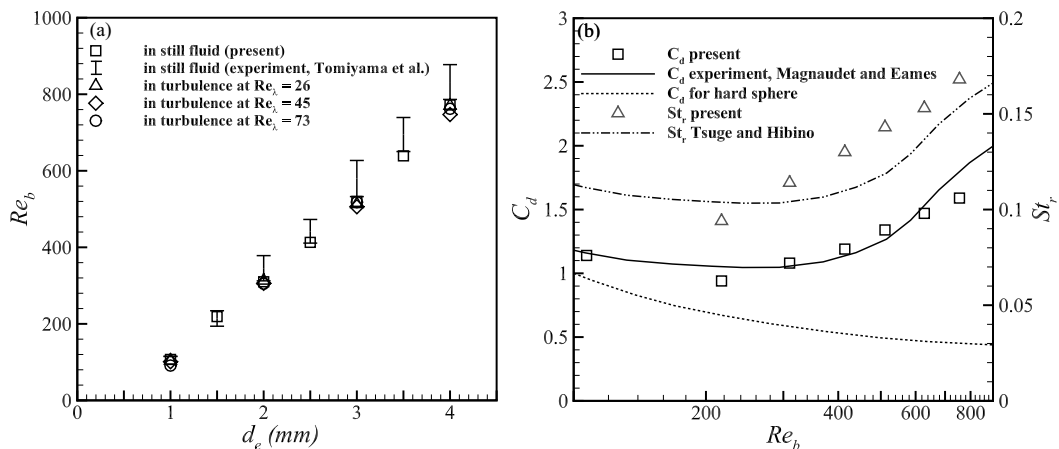
FIG. 2. Comparison against measurement data of (a) the averaged bubble Reynolds number Re_b in still fluid and isotropic turbulence and (b) drag coefficient and Strouhal number. The Reynolds number is compared with experiments conducted in still fluid for the range of the bubble sizes considered in Tomiyama *et al.* [52]. The drag coefficient C_d is compared with measurement data by Magnaudet and Eames [1] and the Strouhal number St_r is compared with an estimated fit given by Tagawa *et al.* [8], Tsuge and Hibino [53].

is 5 to 10 times the equivalent diameter, which is large enough to minimize the effect of periodicity assumption. The number of Lagrangian points N_l depending on the size and the aspect ratio χ is gradually increased due to the size growth of r_a and r_b. In addition to long vertical domain, we applied a tilted gravity by β toward x axis and γ toward y axis so that the gravitational acceleration vector is $\boldsymbol{g} = g(-\sin\beta\cos\gamma, -\sin\gamma, -\cos\beta\cos\gamma)$ for all simulations to minimize the effect of periodicity. $\beta = 0.4$ rad, $\gamma = -0.1$ rad for $1 \sim 3$ mm bubbles and $\beta = 0.3$ rad, $\gamma = -0.1$ rad for 3.5, 4 mm bubbles. Then, all the results are presented in the new coordinate system, X, Y, Z, where gravity acts in the negative Z direction.

Figure 2 provides the bubble Reynolds number Re_b, drag coefficient C_d, and Strouhal number St_r compared with available measurement data. In the prediction of Re_b in Fig. 2(a), overall agreement with the measured data by Tomiyama *et al.* [52] is good although our simulation tends to underpredict the Reynolds number when the bubble size is over 3.0 mm. These errors for large bubbles are probably caused by the fact that the shape of a large bubble is not exactly of spheroid. The upper surface of a large bubble is less convex that the lower surface, breaking the symmetry [52]. Nevertheless, the errors are within 7% for above cases as compared to the lower bound of measurement in the experiments. We also observed that when bubbles are put in three sorts of isotropic turbulence, $Re_\lambda \sim 26$, 45, and 73, the rise velocities for all bubbles do not show any noticeable difference as compared with the bubble in still fluid. The drag coefficient shown in Fig. 2(b) is defined by

$$C_d \equiv \frac{4}{3}\frac{d_e g}{V_T^2},\qquad(28)$$

which is derived by balancing the buoyancy and drag forces [8]. Comparison against measurement by Magnaudet and Eames [1] is excellent. The comparison with the drag coefficient for a hard sphere (dotted line) indicates that the drag coefficient of a bubble starts to deviate from that of a hard sphere as the bubble Reynolds number exceeds around 100 when the path instability sets in. For the cases with path instability, we also compared St_r with an experimental estimate by Refs. [8,53] through C_d in contaminated water as given by
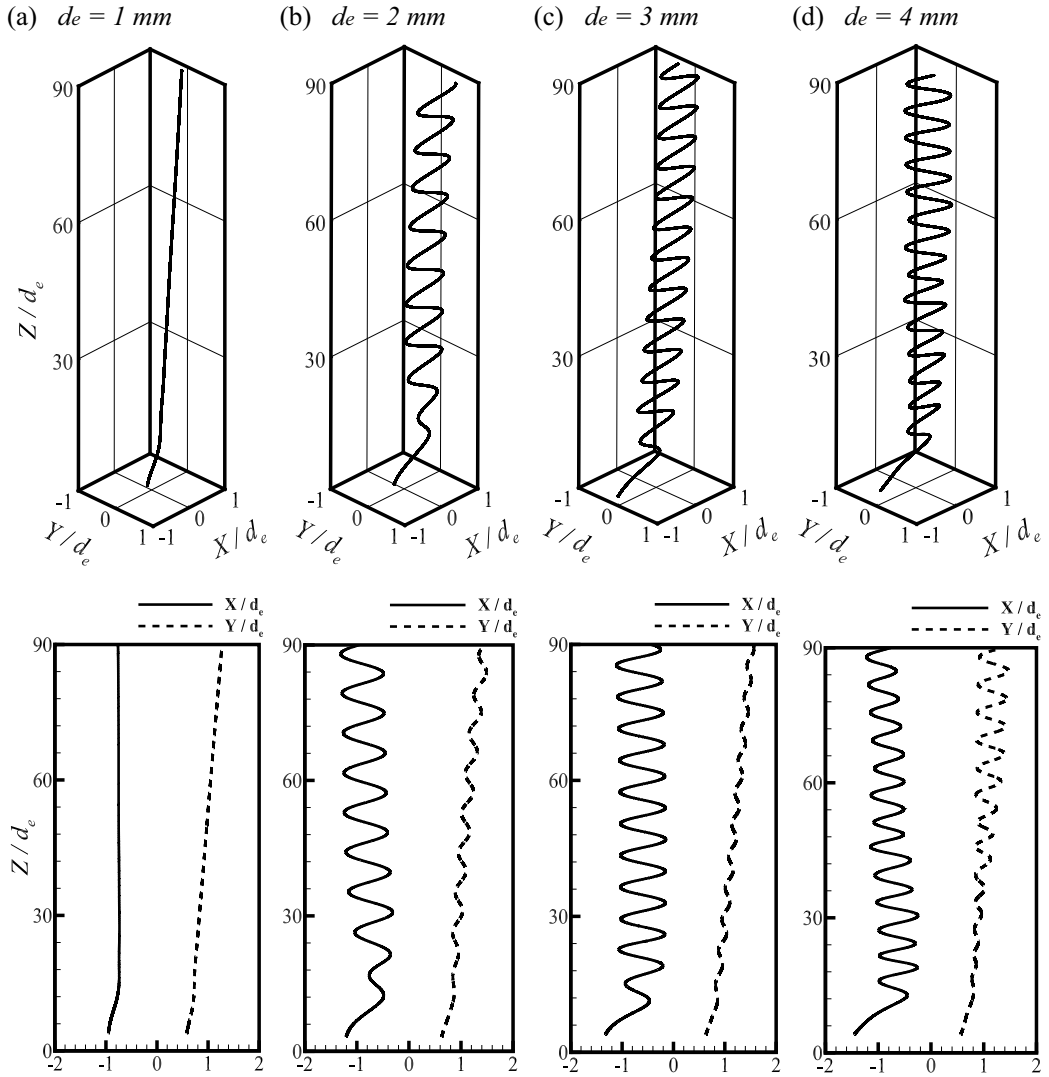
$$St_r = 0.100 C_d^{0.734}.\qquad(29)$$

FIG. 3. Trajectories and horizontal projections of the spheroidal bubble in still fluid for (a) $S - 1.0$, (b) $S - 2.0$, (c) $S - 3.0$, (d) $S - 4.0$. The solid line and the dashed line in the lower panel represent X/d_e and Y/d_e, respectively. A rectilinear motion is observed for $S - 1.0$, and a zigzagging motion can be observed for bubbles larger than 1 mm.

It clearly indicates that although St_r does not show sensitive dependence on the Reynolds number or size, St_r is well fitted by Eq. (29). These good agreements against experimental data confirms that our approach adopting an immersed boundary method to represent the bubble motion as well as utilizing a periodic domain in solving the flow around a single bubble is quite valid.

The trajectories of four different sizes of the bubble with their horizontal projections are presented in Fig. 3, in which each axis is normalized by each bubble's equivalent diameter d_e. When the bubble size is 1.0 mm, as shown in Figs. 3(a) and 3(e), the bubble rises along the rectilinear path without yielding to path instability. Given that all the trajectories are presented in the coordinates (X, Y, Z) where gravity acts in the negative Z direction, all the bubbles are rising in a slightly oblique manner by roughly 5 degrees. This symmetry-breaking behavior of an obliquely rising
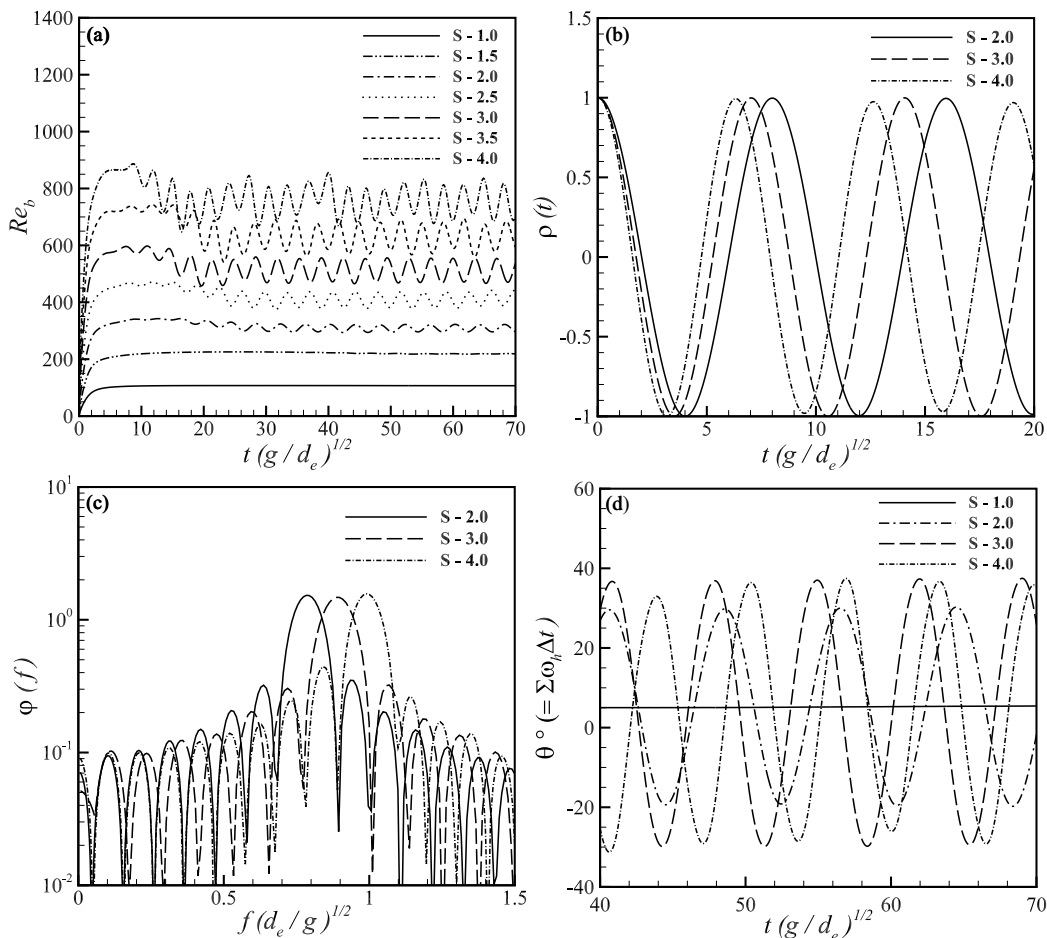
FIG. 4. Statistical results with respect to the bubble's locomotion in still fluid (a) bubble Reynolds number Re_b, (b) two-point autocorrelations of the horizontal velocity ρ_b, (c) conversion frequency spectra φ from the autocorrelations, (d) variation of angle θ along its dominant horizontal direction.

bubble seems to be natural as it was observed in experiments as well [55–57]. As its size becomes greater than 1.0 mm, the bubble shows zigzagging patterns. It has been reported that the critical Reynolds number for the zigzagging patterns in tap or contaminated water is around 202 [1,8,58], which is consistent with our observation that the path instability first occurs for 1.5 mm bubble at $Re_b = 218$. We present the horizontal amplitude of the zigzagging motion in the dominant direction in Table I, indicating that the bubble vacillates over $0.8 \sim 0.9 d_e$ for most cases except the case for $d_e = 1.5$ mm. It is also noticeable that the oscillation plane of the bubble motion is consistently maintained for the bubbles of 2 mm and 3 mm, while the plane becomes twisted as the 4 mm bubble rises.

Various quantities characterizing the zigzagging motion of the bubble are presented in Fig. 4. Figure 4(a) shows instantaneous bubble Reynolds numbers estimated from the rising velocity of the bubble for various sizes, indicating that the rising velocity also oscillates when the bubble shows zigzagging motion. The fluctuations in the bubble Reynolds number are maintained within 5% as the bubble size increases as listed in Table I. Figures 4(b) and 4(c) represent the autocorrelation of the bubble's horizontal velocity $\rho(t)$ and the corresponding frequency spectra φ, which are defined
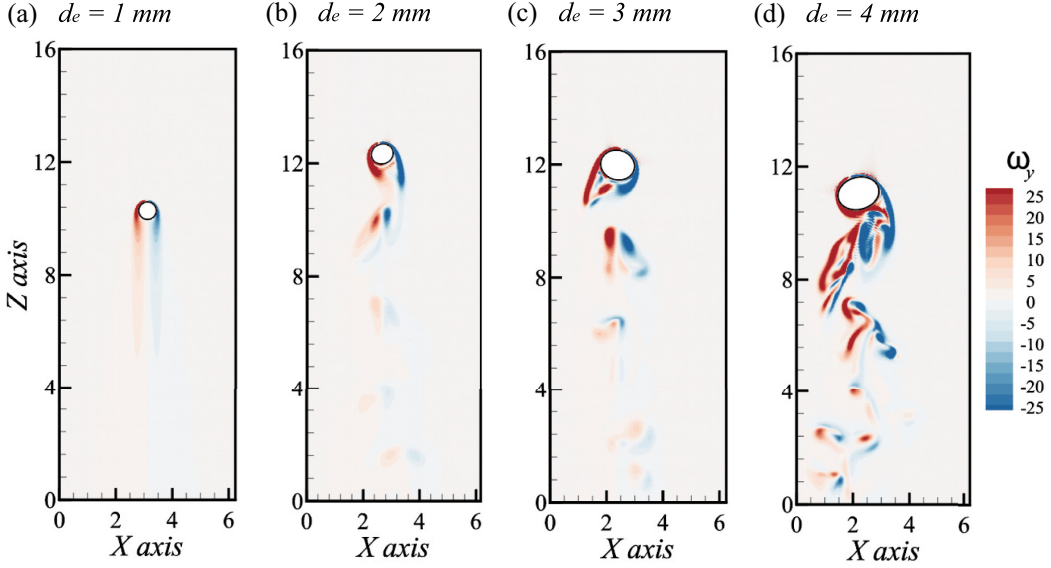
FIG. 5. Instantaneous vorticity contours ω_y around the rising bubble in still fluid for the four cases: (a) $S - 1.0$, (b) $S - 2.0$, (c) $S - 3.0$, (d) $S - 4.0$.

by

$$\rho(t) = \frac{1}{2}\left(\frac{\langle v_x(t_0)v_x(t_0 + t)\rangle}{\langle v_x(t_0)^2\rangle} + \frac{\langle v_y(t_0)v_y(t_0 + t)\rangle}{\langle v_y(t_0)^2\rangle}\right), \quad \varphi(f) = \int_0^{\infty} \rho(t)\cos(ft)dt, \quad (30)$$

where v_x and v_y are the horizontal components of the bubble velocity, respectively. It can be seen from Fig. 4(b) that once the zigzagging motion of the bubble sets in, almost the sinusoidal horizontal motion of the bubble is clear. It is observed that the autocorrelation of bubbles over 2.0 mm oscillate more frequently as the bubble size grows. Figure 4(c) offers converted frequency regimes based on the autocorrelations in Fig. 4(b), which does not show sharp dominant frequency due to the limited time range of the autocorrelations. The dominant frequency, normalized by $(g/d_e)^{1/2}$, increases with the bubble size. Strouhal number St_r in Table I, the frequency normalized by d_e/V_T, also displays the similar tendency with the bubble size. Figure 4(d) presents the angular variation of the bubble's orientation measured from the horizontal component of the bubble's angular velocity, ω_h. Due to the oblique rising motion of 1 mm bubble, the amplitude of the angular variation maintains constant at $5°$, and the angle ranges from $-30°$ to $37°$ as the size grows. In fact, a bubble usually ascends with a little inclination from vertical axis while oscillating perpendicularly to the inclined direction [56].

Figure 5 illustrates the contours of vorticity component ω_y, which is almost orthogonal to the oscillation plane, for the four sizes of the rising bubble. While the symmetric structure of the wake behind 1.0 mm bubble is observed, asymmetric pairs of vortices are found in the wake of bubbles greater than 1 mm due to the zigzagging motion. The wakes are ruffled and further enhanced as the size of the bubble becomes larger. Three-dimensional structure of the wakes is provided in Fig. 6, which shows isosurfaces of enstrophy Ω_{En} $(= \omega_x^2 + \omega_y^2 + \omega_z^2)$ and the vertical component of vorticity ω_z for 2.0 mm and 3.0 mm bubbles. Wakes behind the bubbles moving in the zigzag pattern are composed of bilaterally symmetric tails. Especially, the tails are alternately switched after the horizontal direction of the bubble's motion is changed as shown in Figs. 6(b) and 6(d).
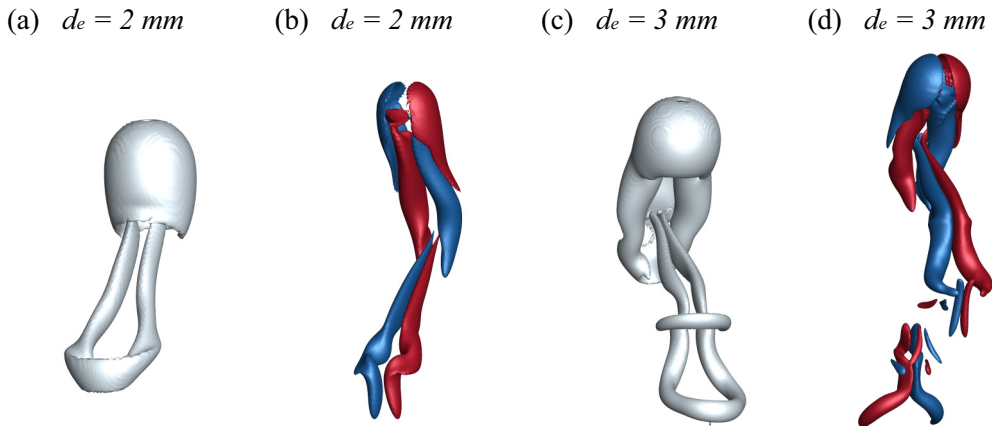
(a) $d_e = 2\ mm$ (b) $d_e = 2\ mm$ (c) $d_e = 3\ mm$ (d) $d_e = 3\ mm$

FIG. 6. Three-dimensional enstrophy structures at Ω_{En} and isovorticity ω_z surfaces around the rising bubble in still fluid for two cases: (a) $S - 2.0$ ($\Omega_{En} = 1600$), (b) $S - 2.0$ ($\omega_z = \pm 15$), (c) $S - 3.0$ ($\Omega_{En} = 1600$), (d) $S - 3.0$ ($\omega_z = \pm 15$). Values of red and blue colors for ω_z have the value of $+15$ and -15, respectively.

IV. BEHAVIOR OF A SPHEROIDAL BUBBLE IN ISOTROPIC TURBULENCE

In bubble-laden turbulence, the interaction between bubbles and turbulence shows quite diverse behavior depending on the relative size of a bubble to the flow length scale. When the bubble size is smaller than the Kolmogorov length scale, the point-bubble approximation has been adopted in most numerical investigations [32,59–62], where the motion of a bubble is passively determined by turbulent fields and the back reaction by the bubbles to turbulence is in many cases negligibly small [63]. However, for a millimetric size bubble, the mutual interaction between the bubble and turbulence needs to be fully considered given that the Kolmogorov length scale is a few hundred microns even in very weak turbulence. In this section, the dynamic behaviors of a spheroidal bubble of various sizes are analyzed in isotropic turbulence of various strengths. The settings of the simulation domain, the sizes of the bubble and the resolutions are the same as those for a single bubble in still fluid in the previous section. Considered range of strength of the background turbulence is $\mathrm{Re}_\lambda = 26$, 45, and 73 and $\kappa_m \eta = 9.89$, 3.78, and 2.58, respectively, where κ_m is the maximum wavenumber and η is the Kolmogorov length scale. Table II lists considered cases with the bubble sizes and the Kolmogorov scales in real units. Although only three different turbulent fields were considered for each size of bubble, the turbulence parameters in real units are all slightly different for the same Re_λ since the size of a bubble relative to the domain length was differently selected for efficient simulation.

Table III lists 16 cases considered in the investigation of the effect of the background turbulence onto the behavior of a bubble including the case in still fluid. For each size of the bubble, the results for three different strengths of turbulence are compared against the case in still fluid. The Kolmogorov length scale ranges between 1/4th and 1/40th of the bubble size while the Taylor micro-scale varies from twice to one half the bubble size. In case of bubbles over 2 mm, the small difference of u'/V_T at the same size and turbulent fluctuation does not cause any noticeable change in the rise velocity in still fluid and considered turbulence. A noticeable effect of turbulence is found for 1 mm bubble, which showed the rectilinear motion in still fluid; turbulence induces the path instability as confirmed in the trajectory shown in Figs. 7(a) due to relatively large value of u'/V_T than other bubbles. Figure 7 displays trajectory of the bubbles of four sizes and its horizontal projection in three different turbulences compared against the case in still fluid. When the bubble size is 1 mm, the strength of turbulence at $\mathrm{Re}_\lambda = 26$ seems so marginal that it induces the path instability while turbulence at $\mathrm{Re}_\lambda = 45, 73$ are strong enough for passive displacement of the bubble by turbulence to dominate the path instability. Actually, we can observe a slight decrease

TABLE II. Cases considered in this study. For real unit conversion, we use $\nu = 0.01$ cm^2/s for water, $g = 981$ cm/s^2. $d_e, \epsilon, \eta, \tau_\eta$ and v_η are the bubble size, the Kolmogorov length scale, the Kolmogorov time scale and the Kolmogorov velocity scale in real units, respectively, which are dependent on the size [44,49]. Due to a restriction of domain sizes, we estimated this by employing the same d_e in Table I, which is not proportional for the bubble size in computer units, so the estimation of real turbulence is different for each case.

Case	Re$_\lambda$	d_e (cm)	ϵ (cm^2/s^3)	η (cm)	τ_η (s)	v_η (cm/s)
$T1 - 1.0$	26	0.1	2.331	0.0255	0.0655	0.3907
$T2 - 1.0$	45		106.3	0.0098	0.0097	1.015
$T3 - 1.0$	73		472.6	0.0068	0.0046	1.474
$T1 - 2.0$	26	0.2	0.5487	0.0367	0.1350	0.2722
$T2 - 2.0$	45		25.00	0.0141	0.0200	0.7071
$T3 - 2.0$	73		110.8	0.0097	0.0095	1.026
$T1 - 3.0$	26	0.3	0.4672	0.0382	0.1463	0.2614
$T2 - 3.0$	45		21.43	0.0147	0.0216	0.6804
$T3 - 3.0$	73		94.26	0.0101	0.0103	0.9853
$T1 - 4.0$	26	0.4	0.2600	0.0443	0.1961	0.2258
$T2 - 4.0$	45		11.89	0.0170	0.0290	0.5872
$T3 - 4.0$	73		52.51	0.0117	0.0138	0.8512

in Re$_b$ in Table III as the turbulence strength increases. It is conjectured that this is contributed from two mechanisms. One is the turbulent fluctuation which triggers the enhancement of the vorticity production on the bubble surface, resulting in pronounced path instability. The other is isotropic turbulent eddies mainly driving the bubble in random direction, reducing the bubble rise velocity. Similar behavior is found for 2 mm bubble while for the bubbles of size 3 and 4 mm, the trajectories

TABLE III. Statistical quantities characterizing the behavior of bubbles in turbulence. The parameters related with bubbles such as Ga and χ are the same as those in Table I for cases in still fluid. $v_h (= (v_{x,rms} + v_{y,rms})/2)$ is the averaged horizontal r.m.s. velocity of the bubble. The bubble sizes are compared against the Kolmogorov length scale η and the Taylor microscale λ. Re$_b$ is the averaged bubble Reynolds number after the bubble reaches statistically stationary state in turbulent flows. The obliquity angle for bubbles in still fluid is different from the range of the angle in the maximum oscillation plane listed in Table I.

| Case	Ga	χ	η/d_e	λ/d_e	u'/V_T	v_h/V_T	Re$_b$	St$_r$	α
$S - 1.0$	99.0	1.03	—	—	0	0.004	107	0	0°
$T1 - 1.0$			0.257	2.369	0.096	0.160	104	0.091	20°
$T2 - 1.0$			0.098	1.312	0.357	0.436	98	0.114	57°
$T3 - 1.0$			0.067	1.141	0.671	0.691	96	0.125	104°
$S - 2.0$	280.1	1.10	—	—	0	0.113	309	0.114	35°
$T1 - 2.0$			0.184	1.700	0.045	0.194	314	0.116	42°
$T2 - 2.0$			0.070	0.942	0.166	0.289	293	0.121	63°
$T3 - 2.0$			0.048	0.819	0.300	0.342	299	0.130	88°
$S - 3.0$	514.6	1.18	—	—	0	0.142	512	0.143	48°
$T1 - 3.0$			0.128	1.180	0.039	0.255	510	0.145	52°
$T2 - 3.0$			0.049	0.654	0.140	0.280	503	0.150	66°
$T3 - 3.0$			0.033	0.568	0.252	0.315	512	0.155	68°
$S - 4.0$	792.5	1.28	—	—	0	0.178	756	0.168	49°
$T1 - 4.0$			0.111	1.025	0.030	0.230	763	0.170	57°
$T2 - 4.0$			0.042	0.567	0.107	0.256	748	0.176	66°
$T3 - 4.0$			0.029	0.494	0.198	0.273	751	0.180	69°
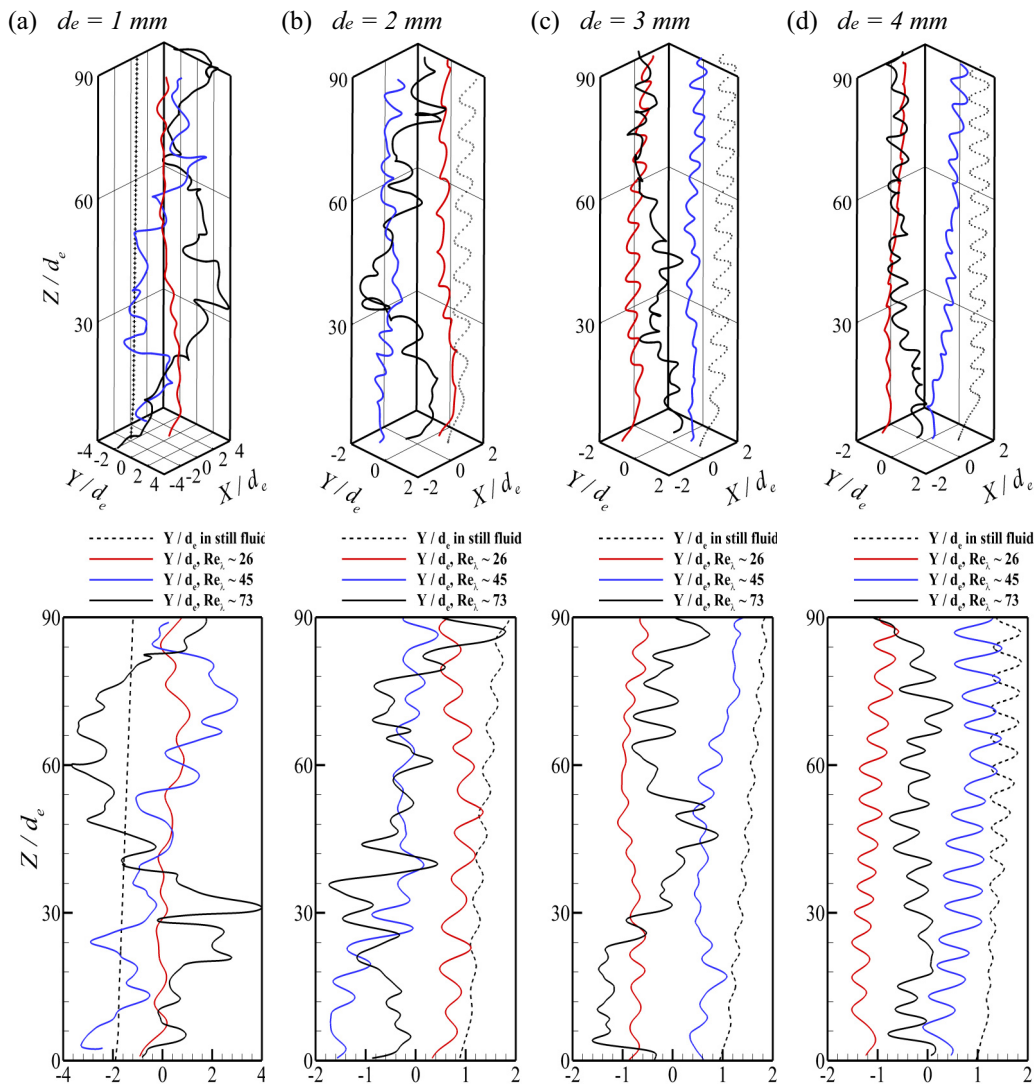
FIG. 7. Trajectories and the horizontal projections of the spheroidal bubble in three kinds of isotropic turbulence at $Re_\lambda = 26$ (red line), 45 (blue line), 73 (black line) compared with cases in still fluid (dashed line) for (a) 1.0 mm bubble, (b) 2.0 mm, (c) 3.0 mm, (d) 4.0 mm, respectively. The lines in lower panel represent Y/d_e.

of the bubble undergoing the path instability are less modified by turbulence. From the investigation of u'/V_T, it can be conjectured that when this ratio is below 0.15, the path instability is hardly influenced by turbulence.

In Fig. 8, we describe the variation of the bubble Reynolds number, the temporal autocorrelation of bubble's horizontal velocity, the corresponding frequency spectra, and the obliquity angle in the horizontal plane for all cases. The variation of instant bubble Reynolds number shown in Fig. 8(a) shows that although the average bubble Reynolds number, or equivalently the average rise velocity of the bubble, is hardly affected by turbulence as confirmed in Table III, the fluctuations for small bubble (2 mm) increase with the strength of turbulence since small bubbles can be more easily manipulated by turbulence. However, it is noticeable that the average bubble Reynolds number for
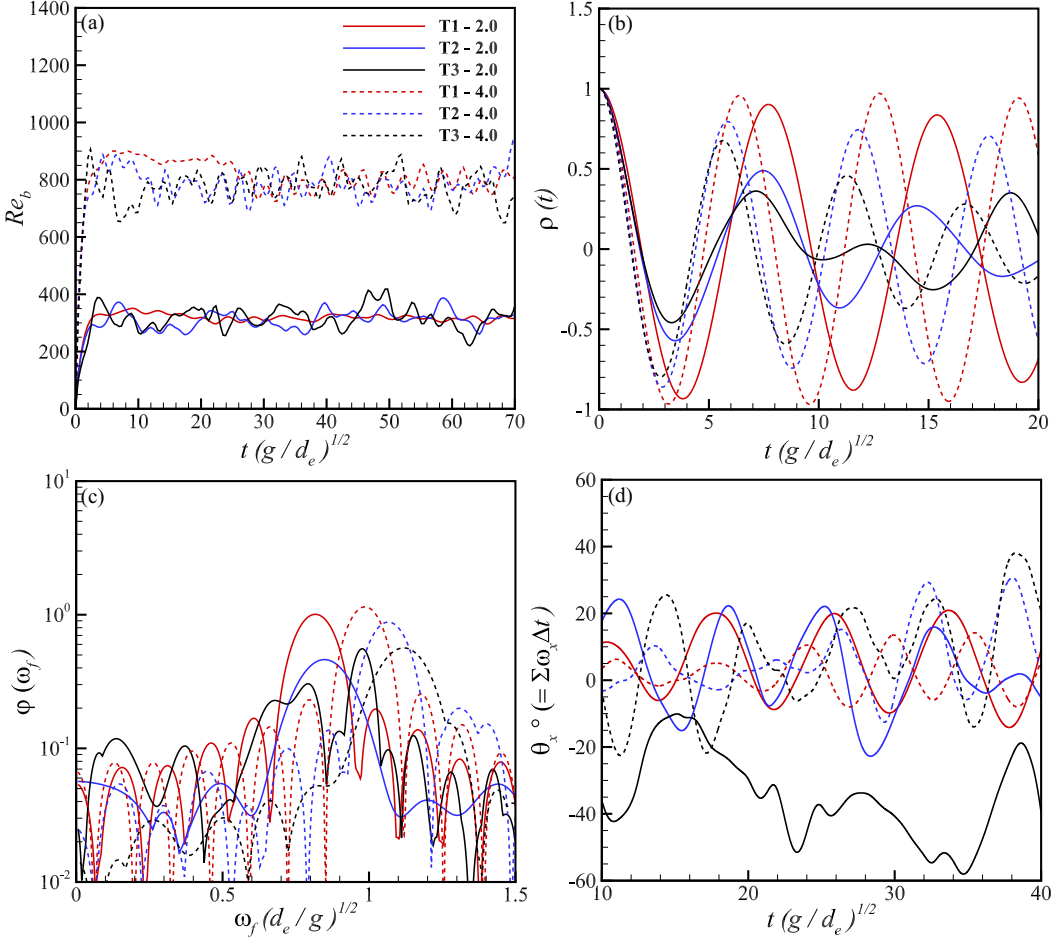
FIG. 8. Statistics of motions for 2.0 mm, 4.0 mm bubbles in turbulence $Re_\lambda = 26, 45, 73$. (a) bubble Reynolds number Re_b, (b) two-point autocorrelations of the horizontal velocity ρ, (c) the frequency spectra φ from the autocorrelations, (d) temporal fluctuation of obliquity angle θ_x about the X direction.

1 mm bubble slightly decreases with the strength of turbulence as shown in Table III. It suggests that the wild zigzagging motion of 1 mm bubble induced by turbulence is responsible for the slight retardation of bubble rising.

The autocorrelation of the bubble's horizontal velocity in turbulence provided in Fig. 8(b) clearly shows decaying behavior compared with those for bubbles in still fluid shown in Fig. 4(b), with this behavior more pronounced for the small bubble (2 mm), for which the path instability is more disrupted by turbulence. The comparison also indicates that turbulence increases the oscillation frequency of the path instability. The corresponding spectrum in Fig. 8(c) confirms this. Between 2 mm bubble and 4 mm bubble, the oscillation frequency normalized by $d_e^{-1/2}$ increases with the size as shown in Figs. 8(b) and 8(c).

The averaged obliquity angle α listed in Table III is defined as follows:

$$\alpha \equiv [(\theta_{x,\max} - \theta_{x,\min}) + (\theta_{y,\max} - \theta_{y,\min})]/2, \tag{31}$$

where $\theta_{x,\max}, \theta_{x,\min}, \theta_{y,\max}$, and $\theta_{y,\min}$ are the largest and smallest angles of the horizontal plane of the bubble estimated by the integral of the corresponding horizontal component of the bubble's angular velocity, $\boldsymbol{\omega}_{c,x}$ and $\boldsymbol{\omega}_{c,y}$. Obviously, turbulence increases the obliquity angle, particularly
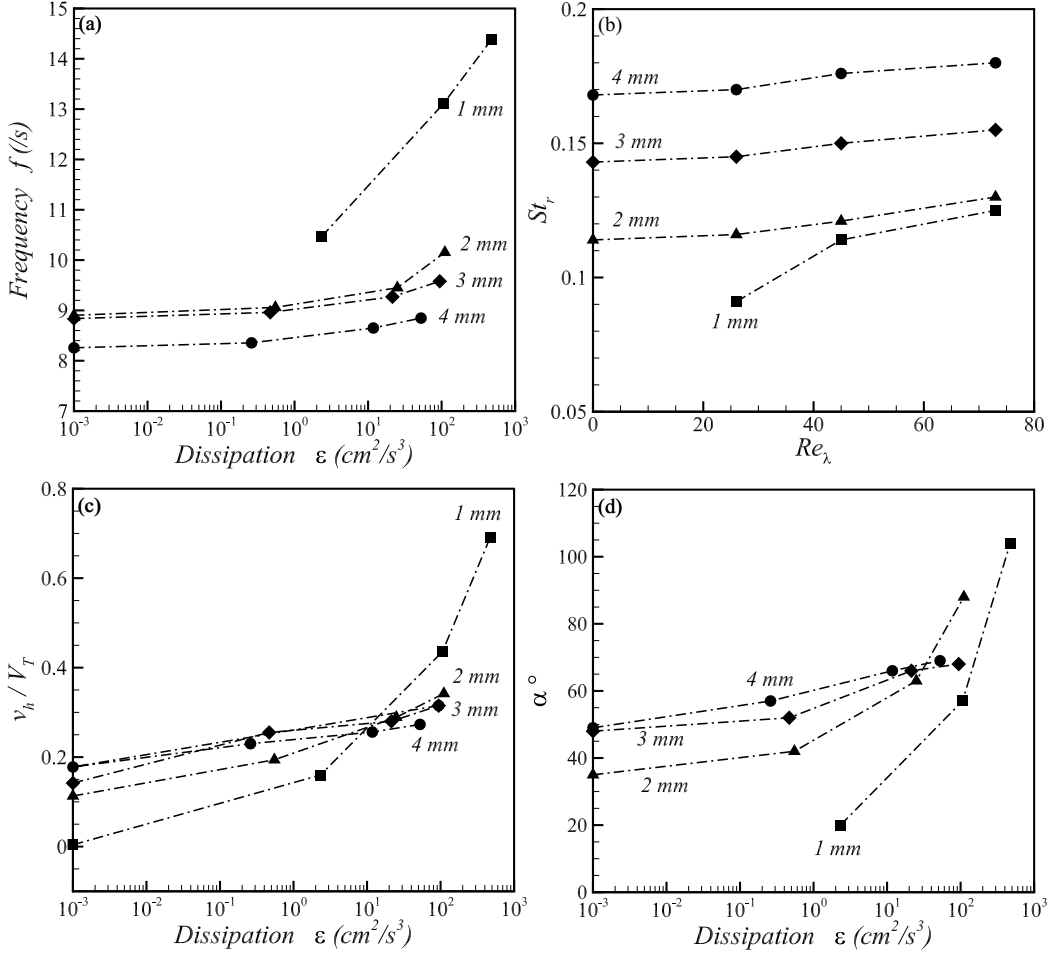
FIG. 9. Various tatistics of bubble locomotion in dissipation ϵ (a) zigzagging frequency f in real unit, (b) Strouhal number St_r in Re_λ, (c) normalized horizontal velocity v_h/V_T, (d) averaged obliquity angle α.

more pronouncing for 1mm bubble. Figure 8(d) shows fluctuations of obliquity angle θ_x of two bubbles 2.0 mm, 4.0 mm for the period of $10 \leqslant t(g/d_e)^{1/2} \leqslant 40$ after the initial transient behavior vanishes. 2.0 mm bubble in the strongest turbulence oscillates around $-40°$, which seems odd. However, since 2 mm bubble's aspect ratio $\xi = 1.10$, proximately spherical, nonspherical shape does not play a role in strong turbulence. Similar behavior was observed for 1 mm bubble (figures not shown). In other cases, the bubble oscillates while maintaining the orientation of spheroid. For the same size of the bubble, the oscillation increases with turbulence strength as shown for 4 mm bubble in Fig. 8(d).

Figure 9 graphically summarizes the effect of turbulence in terms of zigzagging frequency, Strouhal number with Re_λ, normalized horizontal velocity by the rise velocity, the averaged obliquity angle as a function of turbulence dissipation ϵ in real units. Note that for comparison against the case in still fluid, the values of those quantities in still fluid are plotted at $\epsilon = 10^{-3}$ cm^2/s^3 in the log-scale axis. The oscillation frequency in real units increases with the strength of turbulence for all sizes of bubble with 1 mm bubble showing the most rapid increase [Fig. 9(a)], whereas the nondimensional frequency St_r shows much less sensitivity with Re_λ [Fig. 9(b)]. For the similar strength of turbulence, the frequency in real units decreases with the size of bubble while St_r
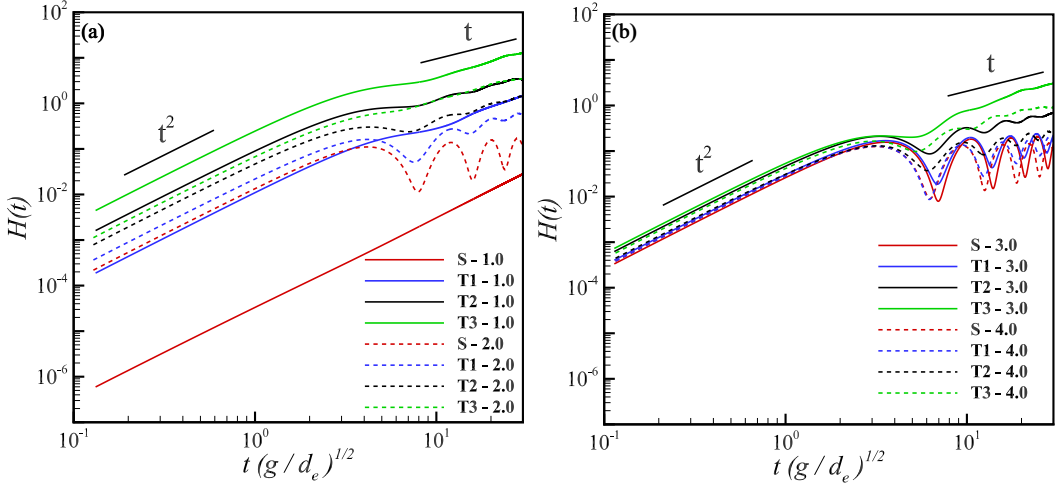
FIG. 10. The horizontal mean-squared dispersion $H(t)$ in time for (a) 1.0 mm, 2.0 mm bubbles, (b) 3.0 mm, 4.0 mm bubbles. $H(t)$ shows a ballistic increase $\sim t^2$ at an early stage and then diffusive $\sim t$ later. The normalized Lagrangian integral time scale in each turbulence for each bubble size, $T_L(g/d_e)^{1/2}$ are 60.5 for $T1 - 1.0$, 7.2 for $T2 - 1.0$, 3.3 for $T3 - 1.0$, 88.0 for $T1 - 2.0$, 10.5 for $T2 - 2.0$, 4.8 for $T3 - 2.0$, 78.0 for $T1 - 3.0$, 9.3 for $T2 - 3.0$, 4.2 for $T3 - 3.0$, 90.5 for $T1 - 4.0$, 10.8 for $T2 - 4.0$, 4.9 for $T3 - 4.0$, respectively.

increases with the size. The horizontal velocity relative to the rise velocity presented in Fig. 9(c) increases slightly with the strength of turbulence except for 1 mm bubble the motion of which is most sensitively affected by turbulence due to its small size. The obliquity angle shown in Fig. 9(d) exhibits similar behavior to the horizontal velocity of the bubble in Fig. 9(c). It clearly demonstrates that the small-size bubbles (1 or 2 mm) are easily manipulated by turbulence.

In Fig. 10, we investigate the horizontal bubble dispersion represented by

$$H(t) = \frac{\langle [x_c(t - t_0) - x_c(t_0)]^2 \rangle + \langle [y_c(t - t_0) - y_c(t_0)]^2 \rangle}{2d_e^2}, \qquad (32)$$

where $x_c(t)$, $y_c(t)$ are horizontal positions of the bubble after the elapsed time $t - t_0$ from the reference instance t_0. For statistical average, the average over all the available reference instances of a single bubble was carried out. 1 mm bubble in still fluid [case $S - 1.0$ in In Fig. 10(a)] displays ballistic behavior all the way since the bubble shows oblique rectilinear motion as shown in Fig. 3. As turbulence induces the path instability, dispersion shows typical behavior of transition from ballistic to diffusive dispersion around $t(g/d_e)^{1/2} \sim 10$. For bubbles 2 mm or larger, the path instability in still fluid or weak turbulence causes oscillatory behavior in dispersion in diffusion stage while strong turbulence tends to suppress this oscillation, which was also reported in Ref. [16] through experiments. While the bubble's motion is predominantly affected by the path instability, the overall level of dispersion is lower than that in strong turbulence. Similar pattern was observed in the behavior of micro-bubbles in stratified turbulence [62]. As the bubble size becomes larger, the dispersion normalized by the size of the bubble tends to approach universal behavior as shown in Fig. 10(b).

Finally, Fig. 11 provides instantaneous vorticity contours ω_y for all cases in turbulence in Table III. Meandering distribution of the wake vortices induced by turbulence can be observed for 1.0 mm bubble at the lowest Re$_\lambda$. In this weak turbulence, the vortices generated by the bubble's motion are much stronger than the background vorticity, whereas they are comparable to each other for the cases in strong turbulence. In very strong turbulence, the wake vortices are indistinguishable although the path of the bubble is slightly discernible for large size bubbles.
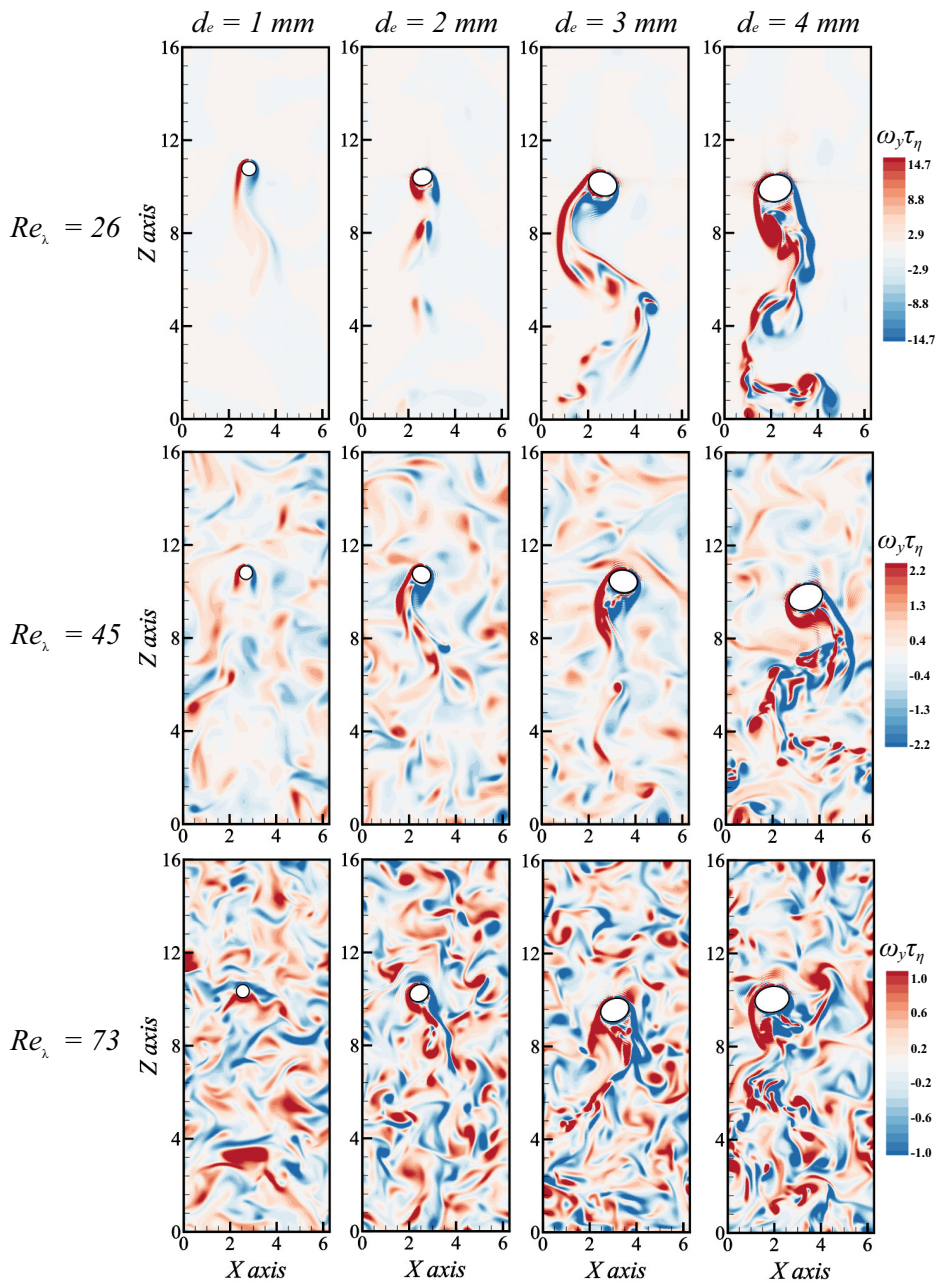
FIG. 11. Instantaneous vorticity contours ω_y of flow around a bubble for 4 sizes in three sorts of isotropic turbulence.

V. CONCLUSION

We numerically investigated path instability of a millimeter-scale air bubble in quiescent fluid and three different strengths of isotropic turbulence. To simulate the interaction between a fully contaminated bubble ranging $1.0 \sim 4.0$ mm in size and the background turbulence, an immersed boundary method was adopted to impose the no-slip boundary condition on the bubble surface. In

solving the governing equations for a bubble, the singularity problem induced by the diminishing density ratio was avoided by adding the virtual mass force to the equation of motion. Considered range of the Galilean number is 100 to 800.

We first described the behavior of a bubble in quiescent fluid. 1.0 mm bubble showed a rectilinear path and the zigzag pattern caused by the path instability was observed for 2.0 mm or larger bubble. To characterize the zigzag motion of a bubble, two-point correlations of bubble's horizontal velocity and the oscillation angle of the bubble's orientation were investigated. The nondimensional frequency of the oscillation, St_r slightly increases with the size of the bubble, which is similar to the result in Ref. [64] in that quicker vortex shedding is triggered by turbulence, exhibiting good agreement with the known empirical formula. The angle variation of the bubble's orientation increases with the bubble size, approaching $\pm 30°$. In addition, we observed that wakes behind bubbles were formed as tails switched alternately after zigzagging occurred.

Then, we investigated the path instability of a bubble in isotropic turbulence with $Re_\lambda \sim 26, 45$, and 73. Due to a relatively large value of u'/V_T, 1 mm bubble revealed pronounced path instability with slightly decreased rise velocity according to an increase in Re_λ. However, the small range of u'/V_T at the same size and the turbulent fluctuation did not cause the significant difference of bubble rise velocity over 2 mm bubble. The zigzagging frequency and averaged obliquity of the bubble increased with the enhancement of turbulence. We also observed that wakes behind the bubble became shorter and tangled at high Re_λ.

Finally, our study is confined to a fully contaminated bubble with fixed shape, on the surface of which the no-slip condition is satisfied. Therefore, more diverse features of a rising bubble such as helical pathways were not observed, which is a typical pattern found for a bubble in pure water. Although the immersed boundary method is effective in describing motions of finite-size particles, the more advancement is still required to handle the more complicated interface conditions. For instance, Schwarz *et al.* [65] tried to utilize an immersed boundary method to observe an impact of flows on bubble shapes. Kempe *et al.* [66] imposed the free-slip boundary condition on a spheroidal particle fixated to center in a domain. With these methods or more advanced algorithm, it could be possible to investigate various features of a millimetric bubble in various conditions in future.

---

[1] J. Magnaudet and I. Eames, The motion of high-Reynolds-number bubbles in inhomogeneous flows, Annu. Rev. Fluid Mech. **32**, 659 (2000).

[2] M. Wu and M. Gharib, Experimental studies on the shape and path of small air bubbles rising in clean water, Phys. Fluids **14**, L49 (2002).

[3] G. Riboux, F. Risso, and D. Legendre, Experimental characterization of the agitation generated by bubbles rising at high Reynolds number, J. Fluid Mech. **643**, 509 (2010).

[4] W. Shew, S. Poncet, and J.-F. Pinton, Path instability and wake of a rising bubble, arXiv:hal-00013378v1 (2005).

[5] K. Lunde and R. J. Perkins, Shape oscillations of rising bubbles, Appl. Sci. Res. **58**, 387 (1997).

[6] C. Veldhuis, A. Biesheuvel, and L. Van Wijngaarden, Shape oscillations on bubbles rising in clean and in tap water, Phys. Fluids **20**, 040705 (2008).

[7] R. Clift, J. R. Grace, and M. E. Weber, *Bubbles, Drops, and Particles* (Dover Publications, New York, 2005).

[8] Y. Tagawa, S. Takagi, and Y. Matsumoto, Surfactant effect on path instability of a rising bubble, J. Fluid Mech. **738**, 124 (2014).

[9] Y. Tagawa, T. Ogasawara, S. Takagi, and Y. Matsumoto, Surfactant effects on single bubble motion and bubbly flow structure, in *The 6th International Symposium on Multiphase Flow, Heat Mass Transfer and Energy Conversion*, edited by L. Guo, D. D. Joseph, Y. Matsumoto, Y. Sommerfeld, and Y. Wang, AIP Conf. Proc. No. 1207 (AIP, New York, 2010), p. 43.

[10] M. K. Tripathi, K. C. Sahu, and R. Govindarajan, Dynamics of an initially spherical bubble rising in quiescent liquid, Nat. Commun. **6**, 1 (2015).

[11] G. Mougin and J. Magnaudet, Path Instability of a Rising Bubble, Phys. Rev. Lett. **88**, 014502 (2001).

[12] W. L. Shew and J. F. Pinton, Dynamical Model of Bubble Path Instability, Phys. Rev. Lett. **97**, 144508 (2006).

[13] G. Mougin and J. Magnaudet, The generalized Kirchhoff equations and their application to the interaction between a rigid body and an arbitrary time-dependent viscous flow, Int. J. Multiphase Flow **28**, 1837 (2003).

[14] J. C. Cano-Lozano, P. Bohorquez, and C. Martínez-Bazán, Wake instability of a fixed axisymmetric bubble of realistic shape, Int. J. Multiphase Flow **51**, 11 (2013).

[15] J. C. Cano-Lozano, C. Martínez-Bazán, J. Magnaudet, and J. Tchoufag, Paths and wakes of deformable nearly spheroidal rising bubbles close to the transition to path instability, Phys. Rev. Fluids **1**, 053604 (2016).

[16] V. Mathai, S. G. Huisman, C. Sun, D. Lohse, and M. Bourgoin, Dispersion of Air Bubbles in Isotropic Turbulence, Phys. Rev. Lett. **121**, 054501 (2018).

[17] J. T. Kim, J. Nam, S. Shen, C. Lee, and L. P. Chamorro, On the dynamics of air bubbles in Rayleigh-Bénard convection, J. Fluid Mech. **891**, A7 (2020).

[18] J. Lu and G. Tryggvason, Dynamics of nearly spherical bubbles in a turbulent channel upflow, J. Fluid Mech. **732**, 166 (2013).

[19] V. Mathai, V. N. Prakash, J. Brons, C. Sun, and D. Lohse, Wake-Driven Dynamics of Finite-Sized Buoyant Spheres in Turbulence, Phys. Rev. Lett. **115**, 124501 (2015).

[20] B. E. Calzavarini, R. Volk, and M. Bourgoin, Acceleration statistics of finite-sized particles in turbulent flow: The role of Faxeén forces, J. Fluid Mech. **630**, 179 (2009).

[21] A. Loisy and A. Naso, Interaction between a large buoyant bubble and turbulence, Phys. Rev. Fluids **2**, 014606 (2017).

[22] V. Mathai, D. Lohse, and C. Sun, Bubbly and buoyant particle laden turbulent flows, Annu. Rev. Condens. Matter Phys. **11**, 529 (2020).

[23] A. D. Cluzeau, G. Bois, A. Toutant, A. D. Cluzeau, G. Bois, and A. T. Analysis, Analysis and modelling of Reynolds stresses in turbulent bubbly up-flows from direct numerical simulations, J. Fluid Mech. **866**, 132 (2020).

[24] S. Takagi and Y. Matsumoto, Surfactant effects on bubble motion and bubbly flows, Annu. Rev. Fluid Mech. **43**, 615 (2011).

[25] V. Eswaran and S. B. Pope, An examination of forcing in direct numerical simulations of turbulence, Comput. Fluids **16**, 257 (1988).

[26] J. Jung, K. Yeo, and C. Lee, Intermittency of acceleration in isotropic turbulence, Phys. Rev. E **77**, 016307 (2008).

[27] Y. Choi, B.-G. Kim, and C. Lee, Alignment of velocity and vorticity and the intermittent distribution of helicity in isotropic turbulence, Phys. Rev. E **80**, 017301 (2009).

[28] A. H. Abdelsamie and C. Lee, Decaying versus stationary turbulence in particle-laden isotropic turbulence: Turbulence modulation mechanism, Phys. Fluids **24**, 015106 (2012).

[29] A. H. Abdelsamie and C. Lee, Decaying versus stationary turbulence in particle-laden isotropic turbulence: Heavy particle statistics modifications, Phys. Fluids **25**, 033303 (2013).

[30] Y. Park and C. Lee, Gravity-driven clustering of inertial particles in turbulence, Phys. Rev. E **89**, 061004(R) (2014).

[31] I. Fouxon, Y. Park, R. Harduf, and C. Lee, Inhomogeneous distribution of water droplets in cloud turbulence, Phys. Rev. E **92**, 033001 (2015).

[32] I. Fouxon, G. Shim, S. Lee, and C. Lee, Multifractality of fine bubbles in turbulence due to lift, Phys. Rev. Fluids **3**, 124305 (2018).

[33] M. Tanaka and D. Teramoto, Modulation of homogeneous shear turbulence laden with finite-size particles, J. Turbul. **16**, 979 (2015).

[34] M. Tanaka, Effect of gravity on the development of homogeneous shear turbulence laden with finite-size particles, J. Turbul. **18**, 1144 (2017).

[35] S. Schwarz, T. Kempe, and J. Fröhlich, A temporal discretization scheme to compute the motion of light particles in viscous flows by an immersed boundary method, J. Comput. Phys. **281**, 591 (2015).

[36] M. N. Ardekani, P. Costa, W. P. Breugem, and L. Brandt, Numerical study of the sedimentation of spheroidal particles, Int. J. Multiphase Flow **87**, 16 (2016).

[37] H. Lee, I. Fouxon, and C. Lee, Behavior of sedimenting ellipsoidal particles in isotropic turbulence (unpublished).

[38] J. Jang, Numerical study of finite-size particle laden turbulent channel flows, Ph.D. thesis, Yonsei University, 2019.

[39] M. D. Shuster and S. D. Oh, Three-axis attitude determination from vector observations, J. Guid. Control Dynam. **4**, 70 (1981).

[40] M. Uhlmann, An immersed boundary method with direct forcing for the simulation of particulate flows, J. Comput. Phys. **209**, 448 (2005).

[41] T. Kempe and J. Fröhlich, An improved immersed boundary method with direct forcing for the simulation of particle laden flows, J. Comput. Phys. **231**, 3663 (2012).

[42] S. Tschisgale, T. Kempe, and J. Fröhlich, A noniterative immersed boundary method for spherical particles of arbitrary density ratio, J. Comput. Phys. **339**, 432 (2017).

[43] V. Tavanashad and S. Subramaniam, Fully resolved simulation of dense suspensions of freely evolving buoyant particles using an improved immersed boundary method, Int. J. Multiphase Flow **132**, 103396 (2020).

[44] K. Yeo, S. Dong, E. Climent, and M. R. Maxey, Modulation of homogeneous turbulence seeded with finite size bubbles or particles, Int. J. Multiphase Flow **36**, 221 (2010).

[45] J. Jang and C. Lee, An immersed boundary method for nonuniform grids, J. Comput. Phys. **341**, 1 (2017).

[46] J. Jang and C. Lee, Modification of turbulence and stratification of stably stratified turbulent channel flows by finite-size particles, Phys. Rev. Fluids **3**, 124309 (2018).

[47] J. J. Derksen, Direct numerical simulations of aggregation of monosized spherical particles in homogeneous isotropic turbulence, AIChE J. **58**, 2589 (2012).

[48] W. Fornari, F. Picano, and L. Brandt, Sedimentation of finite-size spheres in quiescent and turbulent environments, J. Fluid Mech. **788**, 640 (2016).

[49] M. Tanaka, Motion of spherical bubbles in homogeneous shear turbulence, Fluid Dynam. Res. **51**, 035505 (2019).

[50] C. S. Peskin, Numerica: The immersed boundary method, Acta Numerica **11**, 479 (2002).

[51] A. M. Roma, C. S. Peskin, and M. J. Berger, An adaptive version of the immersed boundary method, J. Comput. Phys. **153**, 509 (1999).

[52] A. Tomiyama, G. P. Celata, S. Hosokawa, and S. Yoshida, Terminal velocity of single bubbles in surface tension force dominant regime, Int. J. Multiphase Flow **28**, 1497 (2002).

[53] H. Tsuge and S. Hibino, The onset conditions of oscillatory motion of single gas bubbles rising in various liquids, J. Chem. Eng. Jpn. **10**, 66 (1977).

[54] S. Aoyama, K. Hayashi, S. Hosokawa, and A. Tomiyama, Shapes of single bubbles in infinite stagnant liquids contaminated with surfactant, Exp. Therm. Fluid Sci. **96**, 460 (2018).

[55] E. Alméras, V. Mathai, D. Lohse, and C. Sun, Experimental investigation of the turbulence induced by a bubble swarm rising within incident turbulence, J. Fluid Mech. **825**, 1091 (2017).

[56] E. Kelley and M. Wu, Path Instabilities of Rising Air Bubbles in a Hele-Shaw Cell, Phys. Rev. Lett. **79**, 1265 (1997).

[57] M. Wu and M. Gharib, Path instabilities of air bubbles rising in clean water, arXiv:patt-sol/9804002.

[58] R. Bel Fdhila and P. C. Duineveld, The effect of surfactant on the rise of a spherical bubble at high Reynolds and Peclet numbers, Phys. Fluids **8**, 310 (1996).

[59] I. M. Mazzitelli, D. Lohse, and F. Toschi, On the relevance of the lift force in bubbly turbulence, J. Fluid Mech. **488**, 283 (2003).

[60] I. M. Mazzitelli, D. Lohse, and F. Toschi, The effect of microbubbles on developed turbulence, Phys. Fluids **15**, L5 (2003).

[61] I. M. Mazzitelli and D. Lohse, Lagrangian statistics for fluid particles and bubbles in turbulence, New J. Phys. **6**, 203 (2004).

[62] G. Shim, H. Park, S. Lee, and C. Lee, Behavior of microbubbles in homogeneous stratified turbulence, Phys. Rev. Fluids **5**, 074302 (2020).

[63] H. Shim and C. Lee, Two-way interaction between isotropic turbulence and dispersed bubbles, J. Mech. Sci. Technol. **35**, 1527 (2021).

[64] A. A. Naso, The interaction between a solid particle and a turbulent flow, New J. Phys. **12**, 033040 (2010).

[65] S. Schwarz, T. Kempe, and J. Fröhlich, An immersed boundary method for the simulation of bubbles with varying shape, J. Comput. Phys. **315**, 124 (2016).

[66] T. Kempe, M. Lennartz, S. Schwarz, and J. Fröhlich, Imposing the free-slip condition with a continuous forcing immersed boundary method, J. Comput. Phys. **282**, 183 (2015).